

Constraining the neutron skin of ^{208}Pb with anisotropic flow in Pb+Pb collisions at the LHC

Xin-Li Zhao,^{1,2,3} Xin-Yi Xie,¹ Yuan Li,^{2,3} and Guo-Liang Ma^{2,3,*}

¹College of Science, University of Shanghai for Science and Technology, Shanghai 200093, China

²Key Laboratory of Nuclear Physics and Ion-beam Application (MOE),
Institute of Modern Physics, Fudan University, Shanghai 200433, China

³Shanghai Research Center for Theoretical Nuclear Physics,
NSFC and Fudan University, Shanghai 200438, China

We study neutron-skin effects of ^{208}Pb in Pb+Pb collisions at $\sqrt{s_{\text{NN}}} = 5.02$ TeV using the improved string-melting version of a multi-phase transport model by varying the neutron density distribution. A systematic response is observed in both the initial eccentricities and the anisotropic flow, indicating that neutron-skin effects survive the full transport evolution of heavy-ion collisions. A χ^2 comparison with ALICE data favors small to moderate neutron skin, while large neutron skin is excluded. The similar descriptions provided by zero and moderate neutron skin point to a geometric degeneracy in the current anisotropic flow in Pb+Pb collisions, where anisotropic flow is primarily driven by the overall collision geometry and size, thus lacking extreme sensitivity to the fine details of the nuclear surface profile. This highlights both sensitivity and limitation of constraining neutron-skin properties with flow measurements in Pb+Pb collisions at the LHC.

I. INTRODUCTION

High-energy heavy-ion collisions provide a unique environment for studying strongly interacting matter under extreme conditions. Over the past decades, a coherent picture of the collective behavior of the quark-gluon plasma (QGP) has been established through extensive measurements of bulk particle production and anisotropic flow [1–3]. Beyond the properties of hot QCD matter itself, increasing attention has recently been devoted to the role of nuclear structure, driven by the possibility that intrinsic features of the colliding nuclei may leave measurable imprints on the initial geometry surviving from the subsequent collective evolution [4–9]. Collisions of isobaric systems, such as Ru+Ru and Zr+Zr, have demonstrated measurable sensitivity of flow observables to nuclear deformation and density distributions [10–13], while collisions of oxygen and neon nuclei at RHIC [14] and the LHC [15–17] have opened new possibilities for exploring cluster structure and shape effects in small and intermediate systems. These studies indicate that relativistic heavy-ion collisions can serve as an unconventional but powerful probe of nuclear structures, complementary to those in traditional low-energy nuclear experiments.

In contrast to light nuclei, the structure of heavy nuclei, typically the neutron skin of ^{208}Pb , remains insufficiently constrained. The neutron skin, $\Delta r_{\text{np}} = \sqrt{\langle r_n^2 \rangle} - \sqrt{\langle r_p^2 \rangle}$, is closely related to the density dependence of the nuclear symmetry energy and the equation of state of neutron-rich matter [18–24]. Despite substantial experimental efforts, including parity-violating electron scattering and hadronic probes, the neutron-skin thick-

ness of ^{208}Pb remains subject to significant uncertainties and notable inconsistencies among different determinations [25–28]. The PREX-II experiment reported a relatively large neutron skin, $\Delta r_{\text{np}} \approx 0.283$ fm [25], whereas the CREX measurement, together with constraints from *ab initio* theory calculations and astrophysical observations, favors a considerably thinner neutron skin in the range $\Delta r_{\text{np}} \simeq 0.12\text{--}0.19$ fm [29–33]. This tension, often referred to as the PREX-CREX puzzle, highlights the absence of a precise, universally acceptable method for determining the thickness of the neutron skin of ^{208}Pb [34–38]. This therefore calls for an independent and complementary approach to probe the neutron-skin structure of heavy nuclei. Heavy-ion collisions provide a particularly promising avenue. From the perspective of relativistic heavy-ion collisions, the spatial distributions of nucleons in colliding nuclei directly determine the initial energy density profile of the QGP with event-by-event fluctuations, which in turn drive the generation of anisotropic flow and multi-particle correlations. This naturally raises the question of whether observables measured in Pb+Pb collisions at ultrarelativistic energies at the LHC can provide complementary constraints on the neutron skin, and how robust such constraints are against uncertainties associated with the dynamical final-state evolution of colliding systems.

Addressing this issue requires a unified framework capable of describing relativistic heavy-ion collisions across a broad range of system geometries and sizes. Transport models offer a natural framework for this purpose. They provide a microscopic description of the entire evolution of heavy-ion collisions, from the initial condition to partonic interactions, hadronization, and final-state hadronic rescattering. Among them, a multi-phase transport (AMPT) model [39] has been widely applied to $p+p$, $p+A$, and $A+A$ collisions at RHIC and LHC energies and has been shown to successfully reproduce key anisotropic flow [40–43]. In this work, we employ the improved ver-

*Electronic address: gma@fudan.edu.cn

sion of AMPT, which incorporates several important improvements over earlier implementations and provides a more consistent description of bulk particle production and anisotropic flow across different collision system geometries and sizes [44–47]. We then perform a systematic study of the impact of different neutron-skin configurations of ^{208}Pb on both initial geometric quantities and final-state anisotropic flow in Pb+Pb collisions at $\sqrt{s_{\text{NN}}} = 5.02$ TeV. This work is designed to address two key questions. First, in transport descriptions of large collision systems, can neutron-skin effects robustly survive the entire process of partonic and hadronic evolution? Second, given the dominance of collision geometry and size, to what extent can current experimental data constrain different neutron-skin scenarios within the AMPT framework? Through this analysis, we aim to clarify the extent of both sensitivity and limitation of using anisotropic flow as probes of the neutron skin in relativistic heavy-ion collisions. This is particularly important in large systems where geometric degeneracies can hinder the ability of flow observables to constrain the neutron skin.

The paper is organized as follows. In Sec. II, we introduce the improved AMPT model and the neutron-skin configurations of ^{208}Pb . In Sec. III, we present and discuss our results on initial-state eccentricities and anisotropic flow, and compare them with ALICE measurements in Pb+Pb collisions. Finally, conclusions are drawn in Sec. IV.

II. IMPROVED AMPT MODEL AND NEUTRON-SKIN CONFIGURATIONS

In this work, the string-melting version of AMPT model (AMPT-SM) [39] is employed to simulate Pb+Pb collisions. The AMPT-SM framework provides a microscopic description of the full collision dynamics, including the generation of initial conditions by the Heavy Ion Jet Interaction Generator (HIJING), partonic scatterings described by Zhang’s Parton Cascade (ZPC), hadronization via quark coalescence, and subsequent hadronic interactions modeled by A Relativistic Transport (ART). We use the improved version of AMPT-SM, which incorporates several significant improvements, such as an improved quark-coalescence mechanism [48], modern parton distribution functions for the free proton, impact-parameter-dependent nuclear shadowing, and an updated treatment of heavy-flavor production [44, 45, 49]. Recent studies have shown that these improvements lead to a more consistent description of particle yields, transverse-momentum spectra, and anisotropic flow over a wide range of collision systems and energies [45–47, 50]. The updated framework therefore provides a reliable basis for investigating how initial geometric features are transmitted to the anisotropic flow.

The spatial distributions of protons and neutrons in the ^{208}Pb nucleus are modeled using the Woods–Saxon

TABLE I: Woods–Saxon parameters for the proton and neutron density distributions for different neutron-skin thicknesses Δr_{np} , with $\Delta r_{np} = 0$ taken as the reference configuration. All values are in fm.

a_n	R_n	a_p	R_p	Δr_{np}
0.20	6.69	0.447	6.68	-0.19
0.549	6.624	0.549	6.624	0 [51]
0.56	6.69	0.447	6.68	0.16 [52]
0.70	6.69	0.447	6.68	0.37
0.90	6.69	0.447	6.68	0.74

parameterization,

$$\rho(r) = \frac{\rho_0}{1 + \exp[(r - R_0)/a]}, \quad (1)$$

where ρ_0 is the saturation density, R_0 the nuclear radius, and a the surface diffuseness parameter. Neutron-skin effects are incorporated by assigning different Woods–Saxon parameters to protons and neutrons. The parameter sets used in this work are summarized in Tab. I, corresponding to neutron-skin thicknesses $\Delta r_{np} = -0.19, 0, 0.16, 0.37, \text{ and } 0.74$ fm, with $\Delta r_{np} = 0$ taken as the reference configuration. In practice, different values of Δr_{np} are obtained by varying the neutron diffuseness parameter a_n while keeping the proton distribution fixed, except for the case of $\Delta r_{np} = 0$.

Fig. 1 illustrates the nucleon density $\rho(r)$ distributions of ^{208}Pb for the five neutron-skin configurations considered in Tab. I. The upper panel shows $\rho(r)$ corresponding to different Δr_{np} . The lower panel presents the ratios of $\rho(r)$ for the four nonzero neutron-skin cases to the reference configuration with $\Delta r_{np} = 0$, i.e., $\rho(r)\{\Delta r_{np} \neq 0\}/\rho(r)\{\Delta r_{np} = 0\}$. In the upper panel, $\rho(r)$ decreases monotonically with increasing Δr_{np} , which is physically reasonable. As the neutron skin becomes thicker, the central nucleon density is progressively reduced. In the lower panel, the ratio ranges from 0.9 to 1.05. For configurations with $\Delta r_{np} < 0$, the ratio is greater than 1, indicating a higher central density compared to the reference case. Conversely, for $\Delta r_{np} > 0$, the ratio is less than 1, reflecting a depletion of the central density as the neutron skin increases. These results demonstrate that the neutron-skin variations induce changes across the radial range, confirming that the neutron skin of the nuclear density profile are controlled and physically reasonable. This systematic, monotonic modification of the ^{208}Pb radial structure, while preserving the total nuclear mass, establishes a clear geometric baseline for analyzing initial eccentricities and final-state anisotropic flow.

These density distributions are used to sample the initial nucleon positions in the improved AMPT-SM model. Once the proton and neutron coordinates are generated according to Eq. 1, the model simulates the full dynamical evolution of Pb+Pb collisions. In this way,

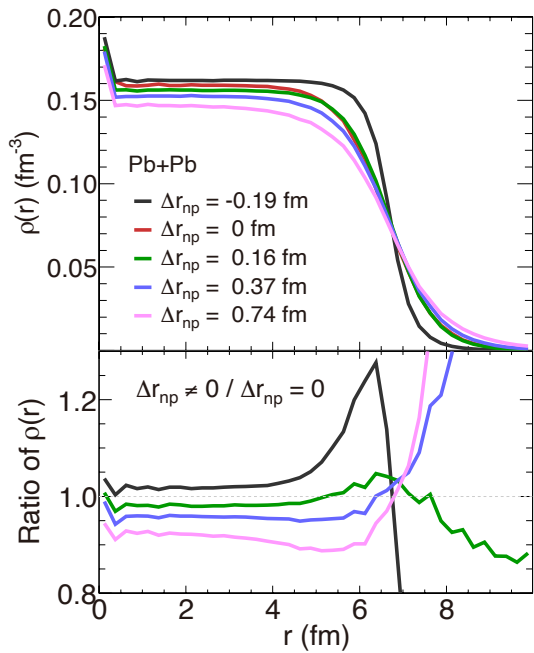


FIG. 1: Upper panel: The nucleon density distributions of ^{208}Pb in Pb + Pb collisions with different Δr_{np} ; Lower panel: The ratio of the nucleon density distributions of ^{208}Pb with Δr_{np} over that without Δr_{np} .

variations in the neutron skin are consistently propagated from the initial nuclear geometry to the final state, enabling a quantitative assessment of the sensitivity of charged-particle multiplicities, mean transverse momentum, anisotropic flow, and flow fluctuations to the neutron-skin structure of ^{208}Pb .

III. RESULTS AND DISCUSSION

A. initial geometry

Fig. 2 and Fig. 3 show the centrality dependence of the initial eccentricities ε_2 and ε_3 [40] for the five neutron-skin configurations of ^{208}Pb . ε_2 and ε_3 are displayed in the upper panels, while the lower panels present the ratios of ε_n for the four nonzero neutron-skin cases to the reference configuration with $\Delta r_{np} = 0$, i.e., $\varepsilon_n\{\Delta r_{np} \neq 0\}/\varepsilon_n\{\Delta r_{np} = 0\}$ and this convention is adopted for all subsequent ratio plots. In this work, centrality is determined from the charged-particle multiplicity distribution measured within $|\eta| < 0.8$ and $0.2 < p_T < 2$ GeV/ c , consistent with the selection used in the ALICE experiment [53].

The neutron-skin effect on ε_2 is shown in Fig. 2, where a clear ordering among the neutron-skin configurations is observed in central and mid-central collisions. Excluding the reference case, more compact nuclei, with smaller or negative Δr_{np} , result in systematically larger elliptic eccentricities, whereas more diffuse neutron distributions

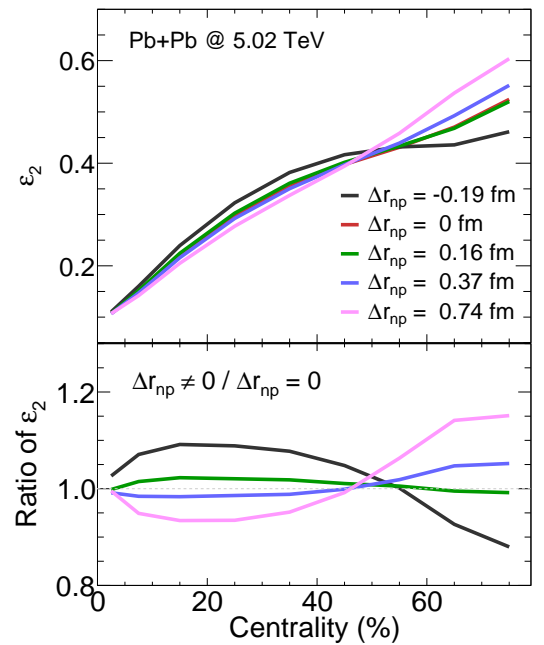


FIG. 2: Upper panel: The centrality dependence of ε_2 in Pb + Pb collisions with different Δr_{np} ; Lower panel: The centrality dependence of the ratio of ε_2 with Δr_{np} over that without Δr_{np} .

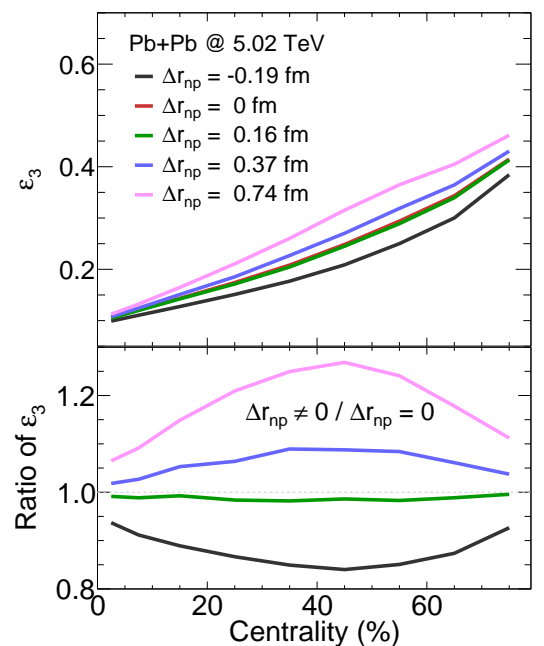


FIG. 3: Upper panel: The centrality dependence of ε_3 in Pb + Pb collisions with different Δr_{np} ; Lower panel: The centrality dependence of the ratio of ε_3 with Δr_{np} over that without Δr_{np} .

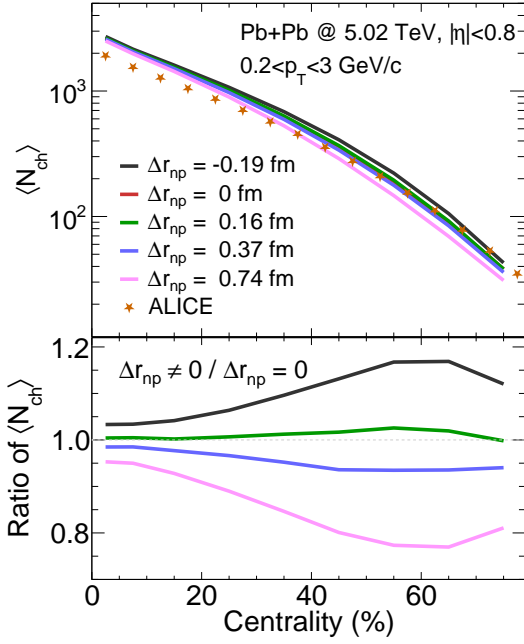


FIG. 4: Upper panel: The centrality dependence of $\langle N_{ch} \rangle$ in Pb + Pb collisions with different Δr_{np} ; Lower panel: The centrality dependence of the ratio of $\langle N_{ch} \rangle$ with Δr_{np} over that without Δr_{np} .

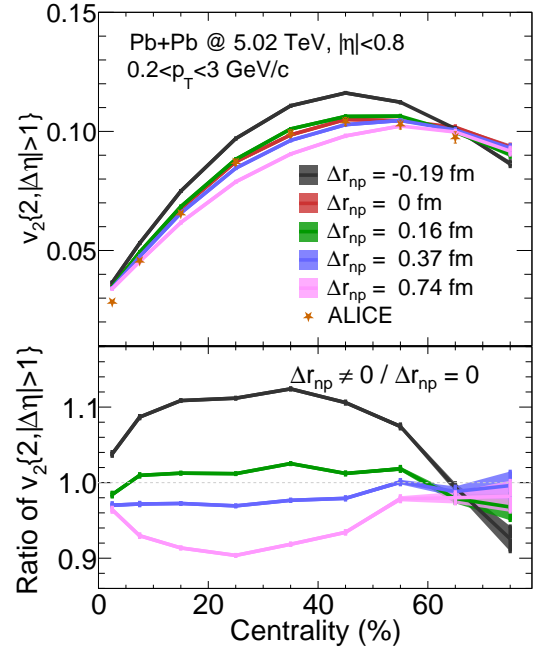


FIG. 6: Upper panel: The centrality dependence of $v_2\{2, |\Delta\eta| > 1\}$ in Pb + Pb collisions with different Δr_{np} ; Lower panel: The centrality dependence of the ratio of $v_2\{2, |\Delta\eta| > 1\}$ with Δr_{np} over that without Δr_{np} .

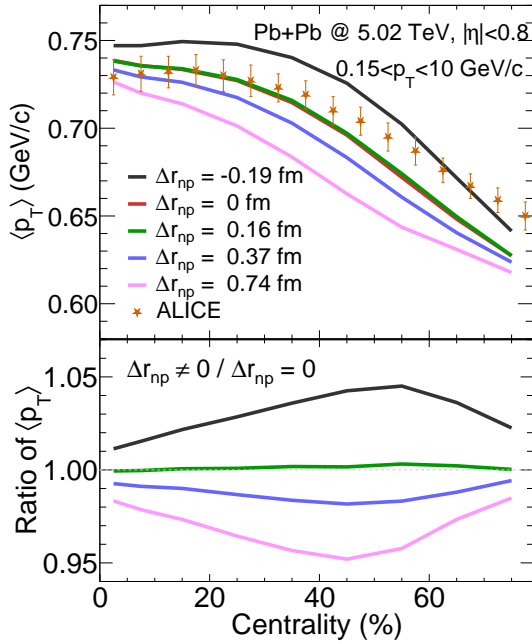


FIG. 5: Upper panel: The centrality dependence of $\langle p_T \rangle$ in Pb + Pb collisions with different Δr_{np} ; Lower panel: The centrality dependence of the ratio of $\langle p_T \rangle$ with Δr_{np} over that without Δr_{np} .

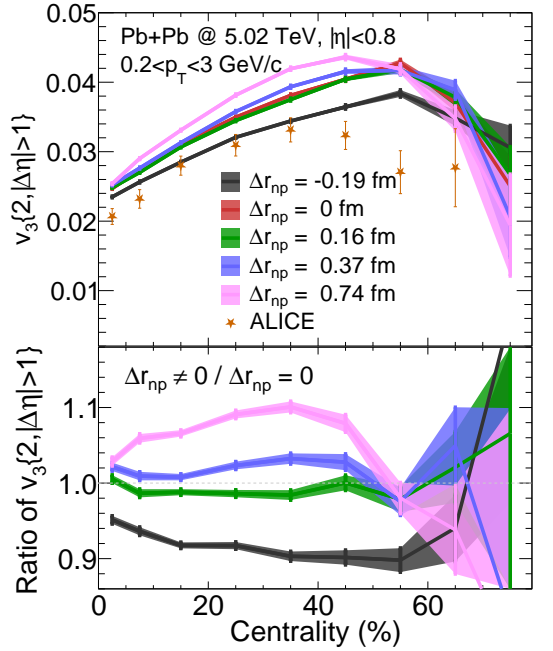


FIG. 7: Upper panel: The centrality dependence of $v_3\{2, |\Delta\eta| > 1\}$ in Pb + Pb collisions with different Δr_{np} ; Lower panel: The centrality dependence of the ratio of $v_3\{2, |\Delta\eta| > 1\}$ with Δr_{np} over that without Δr_{np} .

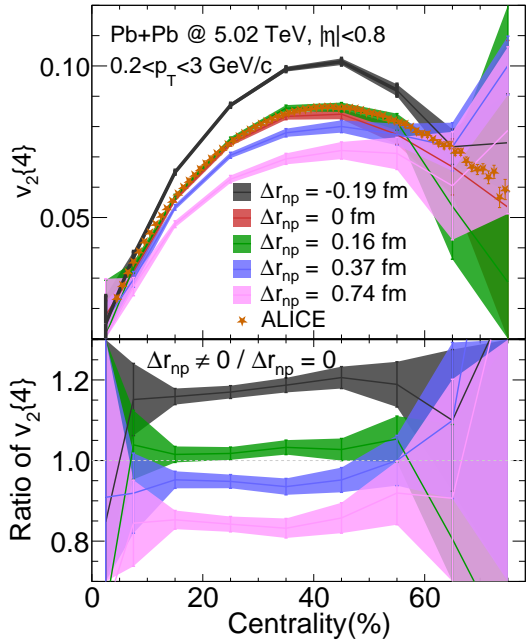


FIG. 8: Upper panel: The centrality dependence of $v_2\{4\}$ in Pb + Pb collisions with different Δr_{np} ; Lower panel: The centrality dependence of the ratio of $v_2\{4\}$ with Δr_{np} over that without Δr_{np} .

suppress ε_2 . This behavior directly reflects the trends of the density profiles shown in Fig. 1, where compact configurations enhance the geometric anisotropy of the overlap region for a given impact parameter. Quantitatively, ε_2 decreases monotonically from the most compact case $\Delta r_{np} = -0.19$ fm to the most diffuse one $\Delta r_{np} = 0.74$ fm over a broad centrality range. In peripheral collisions, however, the ordering is reversed, indicating a transition to a fluctuation-dominated regime in which surface nucleons play a more important role and diffuse density profiles enhance shape irregularities. We further note that the configuration with $\Delta r_{np} = 0.16$ fm remains very close to the reference case over most of the centrality range, which may be attributed to the fact that both configurations have nearly identical root-mean-square nuclear radii, $\sqrt{\langle r^2 \rangle} \approx 5.53$ fm.

A qualitatively different but equally systematic trend is observed for the triangular eccentricity ε_3 . As shown in Fig. 3, ε_3 increases monotonically with increasing neutron skin over the entire centrality range, again excluding the reference configuration. This reflects the growing importance of peripheral nucleons in more diffuse nuclei, which amplifies event-by-event spatial irregularities and thus enhances ε_3 . The near overlap between the $\Delta r_{np} = 0.16$ fm and $\Delta r_{np} = 0$ cases persists also for ε_3 , further supports the idea that moderate neutron-skin effects may be partially obscured by the similarities in initial nuclear geometry resulting from nearly identical nuclear radii.

B. Final-state observables

Fig. 4 presents the charged-particle multiplicity $\langle N_{ch} \rangle$ as a function of centrality for the five neutron-skin configurations, together with the ALICE data [53]. Excluding the reference configuration, $\langle N_{ch} \rangle$ exhibits a clear and monotonic decrease with increasing neutron skin over the full centrality range. This trend is consistent with the dilution of the nuclear overlap region for more diffuse density profiles, which reduces the average participant density in the transverse plane and consequently lowers the entropy deposition and final-state multiplicity. The relative variation is sizable, with ratios spanning approximately 0.75 to 1.2 depending on centrality and neutron-skin thickness. Notably, the configuration with $\Delta r_{np} = 0.16$ fm yields ratios systematically above unity, indicating a modest enhancement compared to the reference geometry. While the model slightly overestimates the multiplicity in the most central events, several configurations reproduce the ALICE data within uncertainties in mid-central and peripheral collisions. While absolute yields from models may not perfectly reproduce experimental data, it is expected that ratios between different configurations can help cancel out such model dependence. These ratios indicate that the centrality dependence of $\langle N_{ch} \rangle$ is sensitive to the neutron skin.

The mean transverse momentum $\langle p_T \rangle$, shown in Fig. 5, follows a similar but weaker trend. Excluding the reference case, $\langle p_T \rangle$ decreases monotonically with increasing Δr_{np} over the full centrality range, reflecting the reduced transverse pressure gradients associated with broader initial energy-density profiles in nuclei with larger neutron skins. In contrast to the strong effect on $\langle N_{ch} \rangle$, the relative variations are small. The $\Delta r_{np} = 0.16$ fm configuration is almost indistinguishable from the reference case, with ratios confined to 0.95–1.05. This indicates that $\langle p_T \rangle$ is only weakly sensitive to neutron-skin effects. The model reproduces the ALICE data [53] well in central collisions, while underestimating the measurements in more peripheral events, pointing to the possible relevance of additional dynamical effects in this region.

The centrality dependence of the two-particle flow coefficients $v_2\{2\}$ and $v_3\{2\}$ for the five neutron-skin configurations is presented in Fig. 6 and Fig. 7, together with the ALICE measurements [54]. For $v_2\{2\}$ in Fig. 6, the results decrease monotonically with increasing Δr_{np} , excluding the reference case, with ratios in the range 0.9–1.1, comparable to the relative variation of the initial ellipticity ε_2 . This close correspondence indicates that the neutron-skin dependence of $v_2\{2\}$ is largely governed by the transformation of the initial geometry. Among the configurations considered, $\Delta r_{np} = 0$ and 0.16 fm provide the best overall description of the data across centrality. In Fig. 7, a qualitatively opposite trend is found for $v_3\{2\}$, which increases monotonically with neutron skin, in line with the behavior of ε_3 . Although the corresponding ratios remain within 0.9–1.1, the overall variation is smaller than that observed for the initial triangular ec-

centricity ε_3 , indicating that the sensitivity to the neutron skin is diluted during the subsequent transport evolution. In comparison with the data, the most compact configuration, $\Delta r_{np} = -0.19$ fm, provides the closest description of $v_3\{2\}$.

Fig. 8 presents the four-particle cumulant elliptic flow $v_2\{4\}$ as a function of centrality. Owing to its strong suppression of nonflow correlations and its direct sensitivity to genuine multiparticle collectivity and event-by-event flow fluctuations, $v_2\{4\}$ offers a stringent test of whether the geometry modifications induced by the neutron skin persist through the full dynamical evolution. A pronounced and systematic dependence on the neutron skin is observed in Fig. 8, excluding the reference case, $v_2\{4\}$ decreases monotonically with increasing Δr_{np} over the entire centrality range, with ratios spanning approximately 0.8–1.2. The magnitude of this variation is comparable to that seen for ε_2 and $v_2\{2\}$, indicating that the neutron skin affects not only the mean elliptic response but also the event-by-event structure of the initial geometry that controls flow fluctuations. The comparison with ALICE data [54] further highlights the discriminating power of $v_2\{4\}$, and the configuration with $\Delta r_{np} = 0.16$ fm provides the best overall agreement, followed by $\Delta r_{np} = 0$, whereas larger neutron skins lead to an increasingly suppressed four-particle cumulant flow. By combining transport model calculations with existing Pb+Pb data, the agreement of both $v_2\{2\}$ and $v_2\{4\}$ on the same small or zero neutron-skin configurations indicates that the neutron skin of ^{208}Pb can be constrained to a relatively narrow range.

C. χ^2 constraint and geometric degeneracy

TABLE II: χ^2 values for different neutron-skin configurations in Pb+Pb collisions.

Δr_{np} (fm)	-0.19	0	0.16	0.37	0.74
χ^2	100.03	3.43	3.67	11.46	70.89

To quantify how current data constrain neutron-skin effects in Pb+Pb collisions, we perform a χ^2 analysis to assess the overall agreement between model calculations and experimental measurements. In our baseline analysis, we construct the χ^2 using observables that are most sensitive to neutron-skin variations, namely $\langle N_{\text{ch}} \rangle$, $v_2\{2\}$, $v_3\{2\}$, and $v_2\{4\}$, and restrict the comparison to the mid-central region 20–60%, where collective flow dominates and exhibits a clear response to geometric variations. The resulting χ^2 values for the five neutron-skin configurations are summarized in Tab. II. For $\Delta r_{np} = -0.19, 0, 0.16, 0.37,$ and 0.74 fm, we obtain $\chi^2 = 100.03, 3.42, 3.67, 11.46,$ and 70.89 , respectively. Among the five cases, the configuration with $\Delta r_{np} = 0$ provides the best overall description of the

ALICE data, followed closely by $\Delta r_{np} = 0.16$ fm, while configurations corresponding to a negative neutron skin or a very large positive neutron skin yield substantially larger χ^2 values and are therefore strongly disfavored by the data. The large χ^2 values obtained for these extreme configurations indicate that such neutron-skin implementations lead to initial geometries and subsequent collective dynamics that are incompatible with the measured observables. In this sense, the comparison with data allows these scenarios to be effectively excluded within the present transport-model framework, even though no single observable alone provides a decisive constraint. We have also examined the χ^2 values obtained under alternative centrality selections or for individual observables. We find that, although the values of χ^2 change in this alternative ways, the relative ordering of χ^2 among different neutron-skin configurations remains unchanged, leading to the same qualitative conclusions.

In contrast, the two preferred configurations with $\Delta r_{np} = 0$ and 0.16 fm yield very similar χ^2 values, indicating that they correspond to nearly equivalent effective collision geometries in Pb+Pb collisions. This near degeneracy can be attributed, at least in part, to the fact that these two cases are characterized by almost identical nuclear root-mean-square radii, which result in very similar transverse density profiles and overlap geometries. For ^{208}Pb , such moderate variations of the neutron-skin thickness therefore induce only limited changes in the global nuclear size and participant geometry, leading to nearly indistinguishable anisotropic flow patterns within the current experimental precision. Our findings indicate that, in large collision systems, the anisotropic flow measurements studied here are primarily influenced by the impact of neutron-skin effects on the collision geometry and size, and they lack extreme sensitivity to the fine details of the nuclear surface profile. Nevertheless, extreme neutron-skin scenarios can be robustly ruled out. However, at the level of current observable data, moderate neutron-skin configurations remain partially degenerate. This calls for either future experimental data with higher statistics or the discovery of experimental observables more sensitive to fine structure of nuclear surface.

IV. SUMMARY

We have carried out a systematic study of neutron-skin effects in Pb+Pb collisions at $\sqrt{s_{\text{NN}}} = 5.02$ TeV within the improved AMPT-SM model. By varying the neutron Woods–Saxon parameters while keeping the proton distribution fixed, a controlled set of configurations spanning $\Delta r_{np} = -0.19$ to 0.74 fm was constructed, and their impact was traced from the initial nuclear density profiles to the final-state anisotropic flow, with direct comparisons to ALICE data. Our results demonstrate that neutron-skin effects are consistently preserved through the full transport evolution. The ordering of the initial eccentricities with Δr_{np} is maintained in the final-

state anisotropic flow, including $v_2\{2\}$, $v_3\{2\}$ and, in particular, the four-particle cumulant $v_2\{4\}$. The pronounced sensitivity of $v_2\{4\}$ indicates that modifications of the participant geometry associated with the neutron skin survive the subsequent partonic and hadronic stages and remain encoded in genuine collective correlations. A quantitative χ^2 analysis shows that current Pb+Pb data exhibit a clear selectivity with respect to neutron-skin variations. Configurations with a negative neutron skin or with a very large neutron-skin thickness are strongly disfavored, while the reference case $\Delta r_{np} = 0$ provides the best overall description of the data, followed closely by $\Delta r_{np} = 0.16$ fm. These two favored configurations cannot be clearly distinguished within the present experimental precision, indicating that moderate neutron-skin variations around the reference Woods–Saxon distribution lead to nearly equivalent descriptions of the measured observables. This behavior reflects the fact that, although anisotropic flow is systematically sensitive to neutron-skin effects, their sensitivity in large collision systems is primarily governed by the collision geometry and size.

As a consequence, different neutron-skin implementations that result in similar effective participant geometries generate nearly indistinguishable anisotropic flow. The present constraints therefore act mainly by excluding extreme neutron-skin scenarios, while leaving a narrow but non-unique region of moderate neutron-skin configurations compatible with the data. Within a transport-model framework, anisotropic flow in Pb+Pb collisions thus provide a robust probe of neutron-skin effects and meaningful discrimination against unphysical or extreme configurations, while residual geometric degeneracy lim-

its a more precise determination of the neutron-skin thickness. This work establishes a systematic and quantitative assessment of how neutron-skin effects are transmitted to anisotropic flow in a transport framework, and clarifies both the sensitivity and the intrinsic limitations of using relativistic heavy-ion collisions to probe nuclear-surface properties. Future progress will benefit from improved experimental precision of multi-particle correlations, observables with enhanced sensitivity to the nuclear surface, and complementary studies in smaller or asymmetric collision systems, which may help to further reduce the remaining geometric degeneracy.

Acknowledgments

We sincerely thank Zi-Wei Lin, Chao Zhang, and Liang Zheng for providing the improved version of the AMPT-SM model and for their substantial contributions to its development and improvement, which were essential for the successful completion of this work. We thank Dr. Chun-Jian Zhang for helpful discussions and Dr. Chen Zhong for maintaining the high-quality performance of Fudan supercomputing platform for nuclear physics. This work is supported by the National Natural Science Foundation of China under Grant No. 12105054 (X.Z.), the National Natural Science Foundation of China under Grants No. 12325507, No. 12547102, and No. 12147101, and the National Key Research and Development Program of China under Grants No. 2022YFA1604900 (G.M.)

-
- [1] J.-Y. Ollitrault, *Phys. Rev. D* **46**, 229 (1992).
 - [2] U. Heinz and R. Snellings, *Ann. Rev. Nucl. Part. Sci.* **63**, 123 (2013), 1301.2826.
 - [3] J. Chen et al., *Nucl. Sci. Tech.* **35**, 214 (2024), 2407.02935.
 - [4] Y.-G. Ma and S. Zhang (2022), 2206.08218.
 - [5] R.-Q. Wang, Y.-H. Li, J. Song, and F.-L. Shao, *Phys. Rev. C* **109**, 034907 (2024), 2309.16296.
 - [6] H. Wibowo and E. Litvinova, *Phys. Rev. C* **100**, 024307 (2019), 1810.01456.
 - [7] D. Gorbunov, D. Kalashnikov, P. Pakhlov, and T. Uglov, *Phys. Lett. B* **843**, 138033 (2023), 2208.03377.
 - [8] J. Jia et al., *Nucl. Sci. Tech.* **35**, 220 (2024), 2209.11042.
 - [9] C. Zhang, J. Chen, G. Giacalone, S. Huang, J. Jia, and Y.-G. Ma, *Phys. Lett. B* **862**, 139322 (2025), 2404.08385.
 - [10] J.-f. Wang, H.-j. Xu, and F.-Q. Wang, *Nucl. Sci. Tech.* **35**, 108 (2024), 2305.17114.
 - [11] X.-L. Zhao, G.-L. Ma, and Y.-G. Ma, *Phys. Rev. C* **99**, 034903 (2019), 1901.04151.
 - [12] X.-L. Zhao and G.-L. Ma, *Phys. Rev. C* **106**, 034909 (2022), 2203.15214.
 - [13] C. Zhang and J. Jia, *Phys. Rev. Lett.* **128**, 022301 (2022), 2109.01631.
 - [14] S. Huang (2023), 2312.12167.
 - [15] I. J. Abualrob et al. (ALICE) (2025), 2509.06428.
 - [16] A. Hayrapetyan et al. (CMS) (2025), 2510.02580.
 - [17] G. Aad et al. (ATLAS) (2025), 2509.05171.
 - [18] X. Roca-Maza, M. Centelles, X. Vinas, and M. Warda, *Phys. Rev. Lett.* **106**, 252501 (2011), 1103.1762.
 - [19] M. B. Tsang et al., *Phys. Rev. C* **86**, 015803 (2012), 1204.0466.
 - [20] B. T. Reed, F. J. Fattoyev, C. J. Horowitz, and J. Piekarewicz, *Phys. Rev. Lett.* **126**, 172503 (2021), 2101.03193.
 - [21] F. Sammarruca, *Phys. Rev. C* **105**, 064303 (2022), 2203.09753.
 - [22] G. F. Burgio, H. C. Das, and I. Vidaña, *Front. Astron. Space Sci.* **11**, 1505560 (2024), 2410.15856.
 - [23] G. Pihan, A. Monnai, B. Schenke, and C. Shen (2025), 2509.21644.
 - [24] T. Suzuki, *PTEP* **2022**, 063D01 (2022), 2204.11013.
 - [25] D. Adhikari et al. (PREX), *Phys. Rev. Lett.* **126**, 172502 (2021), 2102.10767.
 - [26] X. Roca-Maza, M. Centelles, X. Viñas, M. Brenna, G. Colò, B. K. Agrawal, N. Paar, J. Piekarewicz, and D. Vretenar, *Phys. Rev. C* **88**, 024316 (2013), 1307.4806.

- [27] S. P. Malace et al., Phys. Rev. Lett. **106**, 052501 (2011), 1011.4483.
- [28] S. Tagami, T. Wakasa, and M. Yahiro (2023), 2306.09609.
- [29] P.-G. Reinhard, X. Roca-Maza, and W. Nazarewicz, Phys. Rev. Lett. **127**, 232501 (2021), 2105.15050.
- [30] B. Hu et al., Nature Phys. **18**, 1196 (2022), 2112.01125.
- [31] H. Sotani and T. Naito, Phys. Rev. C **107**, 035802 (2023), 2303.03631.
- [32] R. Essick, I. Tews, P. Landry, and A. Schwenk, Phys. Rev. Lett. **127**, 192701 (2021), 2102.10074.
- [33] Z. Zhang and L.-W. Chen, Phys. Rev. C **108**, 024317 (2023), 2207.03328.
- [34] Q. Liu, S. Zhao, H.-j. Xu, and H. Song, Phys. Rev. C **109**, 034912 (2024), 2311.01747.
- [35] M.-Q. Ding, D.-Q. Fang, and Y.-G. Ma, Nucl. Sci. Tech. **35**, 211 (2024), 2409.07059.
- [36] T.-G. Yue, L.-W. Chen, Z. Zhang, and Y. Zhou, Phys. Rev. Res. **4**, L022054 (2022), 2102.05267.
- [37] P. N. Huan, Phys. Rev. C **110**, L051602 (2024), 2405.19018.
- [38] G. Giacalone, G. Nijs, and W. van der Schee, Phys. Rev. Lett. **131**, 202302 (2023), 2305.00015.
- [39] Z.-W. Lin, C. M. Ko, B.-A. Li, B. Zhang, and S. Pal, Phys. Rev. C **72**, 064901 (2005), nucl-th/0411110.
- [40] X.-L. Zhao, Z.-W. Lin, Y. Zhou, C. Zhang, and G.-L. Ma, Phys. Lett. B **874**, 140254 (2026), 2404.09780.
- [41] A. Bzdak and G.-L. Ma, Phys. Rev. Lett. **113**, 252301 (2014), 1406.2804.
- [42] G.-L. Ma and Z.-W. Lin, Phys. Rev. C **93**, 054911 (2016), 1601.08160.
- [43] X.-L. Zhao, Z.-W. Lin, L. Zheng, and G.-L. Ma, Phys. Lett. B **839**, 137799 (2023), 2112.01232.
- [44] C. Zhang, L. Zheng, S. Shi, and Z.-W. Lin, Phys. Rev. C **104**, 014908 (2021), 2103.10815.
- [45] C. Zhang, L. Zheng, F. Liu, S. Shi, and Z.-W. Lin, Phys. Rev. C **99**, 064906 (2019), 1903.03292.
- [46] C. Zhang, Z.-W. Lin, L. Zheng, and S. Shi, in *11th International Conference on Hard and Electromagnetic Probes of High-Energy Nuclear Collisions: Hard Probes 2023* (2023), 2309.01215.
- [47] Z.-W. Lin and L. Zheng, Nucl. Sci. Tech. **32**, 113 (2021), 2110.02989.
- [48] Y. He and Z.-W. Lin, Phys. Rev. C **96**, 014910 (2017), 1703.02673.
- [49] C. Zhang, L. Zheng, S. Shi, and Z.-W. Lin, Phys. Lett. B **846**, 138219 (2023), 2210.07767.
- [50] L. Zheng, C. Zhang, S. S. Shi, and Z. W. Lin, Phys. Rev. C **101**, 034905 (2020), 1909.07191.
- [51] C. Loizides, J. Kamin, and D. d'Enterria, Phys. Rev. C **97**, 054910 (2018), [Erratum: Phys.Rev.C 99, 019901 (2019)], 1710.07098.
- [52] G. Nijs and W. van der Schee (2023), 2304.06191.
- [53] S. Acharya et al. (ALICE), Phys. Lett. B **793**, 420 (2019), 1805.05212.
- [54] S. Acharya et al. (ALICE), JHEP **07**, 103 (2018), 1804.02944.